Electrical conductivity of Sn at high pressure and temperature

Ryan S. Crum, David A. Brantley, Vu Tran, Minta C. Akin, and Ricky Chau

Phys. Rev. B **104**, 184117 — Published 29 November 2021

DOI: 10.1103/PhysRevB.104.184117

Electrical Conductivity of Sn at High Pressure and Temperature

Ryan S. Crum[1],* David A. Brantley[1], Vu Tran[2], Minta C. Akin[1], and Ricky Chau[1]
[1] *Lawrence Livermore National Laboratory, Livermore, CA 94550, USA and*
[2] *Mission Support and Test Services, Livermore, CA 94551, USA*
(Dated: November 9, 2021)

To date, temperature and conductivity have many outstanding implications in extreme environments but are yet to be fully understood under high pressure and temperature dynamic conditions. Here, we introduce a new approach to provide high quality electrical conductivity results under dynamic loading conditions. New emphasis is given to address the skin depth effect's influence in a dynamic loading experiment by using thin films. The thin film samples in this study were at least 100 times thinner than previous samples in dynamic electrical conductivity experiments, increasing the current density to its full potential across the sample's entire cross-section. Consideration of the skin depth accounts for at minimum a 4x scaling factor to the final electrical conductivity result that has neglected in previous dynamic electrical conductivity studies. We also obtained improved signal-to-noise with custom diagnostics optimized for better electrical impedance matching. These considerations were applied to Sn to assess electrical conductivity at elevated pressure and temperature. The high signal-to-noise with reduced skin depth influence results in Sn allow observation of the conductivity changes related to solid-to-solid and solid-to-liquid phase transitions. Additionally, we calculate the Sn thermal conductivity using the Wiedemann-Franz Law for our experiments and compare agains thermal transport dependent temperature measurements from previous work.
keywords: electrical conductivity, electrical resistivity, skin depth, phase boundary, shock, temperature measurement, Wiedemann-Franz

I. INTRODUCTION

Electrical conductivity (σ) of materials under extreme pressure (P) and temperature (T) conditions may provide the necessary information to obtain bulk temperatures via the Wiedemann-Franz Law, the location of phase boundaries, and pertinent knowledge for ongoing electromagnetic responses for planetary interiors.[1–12] We introduce a means to study the electrical conductivity of metals, under elevated P-T conditions and apply our method to measure the electrical resistivity of tin. A plate impact methodology is used to drive the tin sample to high P-T states while the electrical resistivity and conductivity of the sample are recorded.

Researchers have used first principles calculations to predict the melt boundary and electrical conductivity of tin. Bernard and Maillet[13] had success calculating a melt curve and Hugoniot of tin using first principles molecular dynamic simulations. The success of electrical conductivity simulations is elusive and harder to validate. Studies have utilized various methodologies, including DFT, first principles molecular dynamics, and other techniques to ascertain the electrical conductivity.[9,10,14–16] These works often give vastly different responses due to a limited number of experimental results to constrain them.[8,12,17–20]

In a laboratory setting, high P-T regimes are generated using (1) DAC and dynamic shock studies by (2) explosively driven shock, (3) plate impact / gas gun, (4) laser shock, and (5) pulsed power.

DAC has proven to be a useful tool in measuring electrical conductivity at elevated P-T. Most works have tested samples below 15 GPa and 2300 K,[21–28] while other studies have pushed the boundaries of DAC to nearly 200 GPa and 3500 K.[4,5,7,29–36] Compared to shock studies, DAC has significantly longer measurement times but are limited in the upper bound of sample temperature. Resistive and laser heating in DAC typically can reach temperatures up to 1300 K and 5000 K,[37,38] respectively, although larger temperatures (> 8000 K) have been reported.[39,40] Though DAC is a valuable tool, another approach is necessary to further constrain the electrical resistivity and conductivity at elevated P-T, especially one capable of routinely exceeding 5000 K.

Dynamic studies have shown the capability to routinely exceed 5000 K and reach high pressures for a duration of a few ns to hundreds of μs, depending upon the dynamic platform. In these studies, pressure and density typically have error bars $< 5\%$ while temperature has historically had error bars $> 20\%$, with recent studies refining the process to reduce the error bars to $\sim 10\%$.[41]

In 1969, Keeler[42] established requirements to address the electrical conductivity and resistivity under dynamic conditions for insulators, semiconductors, and metals. Keeler's paper has been the basis for all the resulting dynamic studies on gases and liquids,[6,43–54] insulators,[55,56] and metals.[9,42,57–59]Plate impact and explosively driven shock are the commonly employed methodologies for the dynamically loaded electrical conductivity shock experiments. To date, lasers have not been employed due to their short duration, on the order of tens of nanoseconds, limiting time to record the sample's electrical conductivity in a steady state.

There are two significant concerns with previous shock studies of metal electrical conductivity. The first is a low signal-to-noise ratio in experimental signals, limiting accuracy while increasing error bars. This is directly related to a metal's characteristically low electrical re-

* crum3@llnl.gov

sistivity. Second, the skin depth of the sample under dynamic loads was neglected in these studies. Under a dynamic and changing load, current flows through a thin skin at the material surface and not in the interior. Measurements using thick samples will undercount the true current density as the effectively non-conductive volume of the interior is included in the calculation of the current density, as shown in Fig. 1. For example, iron loaded via a plate impact experiment could yield a sample resistance change with an upper bound of 1 GHz. In iron, a 1 GHz frequency would result in a skin depth of $\sim 0.225\ \mu m$,[60] more than two orders of magnitude thinner than samples in prior experiments that were 250 μm and 500 μm.[42,57,58] Thus, the skin depth can play a substantial role, leading to a significantly smaller effective sample cross-section, as shown in Fig. 1. If skin depth is not accounted for during analysis, the resulting sample resistivity will incorrectly be too large while the electrical conductivity will be too small. This may explain observed differences in shock and DAC studies in Fe. The skin depth and low signal-to-noise of prior experiments[42,57,58,61] need to be addressed to determine metals' electrical conductivity.

Detecting phase changes at high P-T is important to understand material response, without the need for specialized diagnostic facilities. X-ray diffraction directly measures in-situ phase, but requires high flux synchroton X-ray sources coupled with a dynamic compression platform.[62] Such facilities are state-of-the-art, and thus to date, measurements are uncommon. More accessible techniques such as Hugoniot[63] and sound speed[64,65] measurements contain averaged phase information across relatively long time scales. In contrast, in the electrical conductivity measurement, the current travels nearly instantaneously through the sample and probes the entire sample. Hence, electrical conductivity may be a more robust method to determine phase changes.

Electrical conductivity also gives insight into thermal conductivity (κ) through Wiedemann-Franz Law. The Wiedemann-Franz Law is $\frac{\kappa}{\sigma} = LT$, where L is the Lorenz number for Sn, 2.49 x 10^{-8} $W\Omega/K^2$.[66] Obtaining bulk temperatures is crucial for the EOS of a material. In shock studies, the most common T measurements are via optical methods (e.g. pyrometry). In opaque materials such as metals, one can only can capture the surface temperature from optical methods. Thermal conductivity is poorly constrained by experiments at elevated P-T, but is essential to convert surface to bulk T.

In this work, we provide significant improvements upon previous studies on metals to address the in-situ electrical resistivity and conductivity of tin. These improvements include addressing the skin depth effect, implementing a well defined and clean ground, and improved electronics for electrical impedance matching that provide results with reduced noise and smaller error bars than previous studies. With these high fidelity signals, we address the electrical resistivity and conductivity at elevated P-T including associated changes with solid-to-solid and solid-to-liquid phase transitions.

II. METHODS

II.1. Electrical Conductivity Diagonostic

The electrical conductivity diagnostic has improved electrical components capabilities to reduce noise issues present in previous works.[57,61] High P-T conditions were achieved using the two-stage light gas guns at the High Energy Application Facility (HEAF) at Lawrence Livermore National Laboratory and the University of California Davis Shock Lab (UCDSL). HEAF fielded shot numbers 4400, 4408, 4409, and 4439, while UCDSL fielded shot numbers 018 and 019. Both facilities have well studied and clean ground signals, essential for these experiments. Additionally, experiments at HEAF maintained all diagnostics and cables in a Faraday cage to minimize sporadic noise during an experiment.

This study implements a 4 probe measurement technique[67] to determine the resistance across the sample. As shown in Fig. 2(a), this measurement technique was accommodated by a specially shaped sample through masked deposition on an Al_2O_3 anvil. The shape consisted of a bar, 10 mm long x 4 mm wide, attached at its ends to two 5 mm wide strips, connecting the bar to the four leads. The leads for the voltage were on opposite sides of the bar's length as were the current leads to ensure the voltage and current flows are measured across the bar's length. Additional information on the triggering and diagnostics in the conductivity measurement system can be found in the supplemental materials.[60]

Figure 3 shows the voltage, current, and trigger at ambient conditions. The capacitor's output lasts for > 100 μs while the experiment lasts < 1 μs, shown as the red box in Fig. 3(a) and enlarged in Fig. 3(b). The current measured by the Rogowski coil voltage remains at 312 $\pm$ 0.7 mV (3.12 $\pm$ 0.007 A). 0.7 μs before pin trigger accounts for the longest possible duration of the experiment with the pins triggering after the experiment is finished.

The sample resistance (R) was determined by Ohm's Law. Given a constant current (I) for the experiment duration, changes in the observed voltage signal (V) were directly related to changes in the sample's resistance.

II.2. Skin Depth

Figure 1 shows how the skin depth effect can strongly influence dynamic resistivity measurements. Even though the discharging capacitor supplies a steady direct current, a change in the sample resistance under dynamic loading will induce eddy currents in response to the change of current flow, creating the skin depth effect. This reduces the sample's cross-section where the current flows.

To address the skin depth effect, we calculated the skin depth (δ) of tin at an upper bound of 1 GHz to be $\sim$ 13.5 μm.[60] To ensure the sample thickness (h_0) is entirely within its skin depth, we deposited tin films of ~ 2 μm. Sample thicknesses $<< 2\delta$ minimize the influence of

the skin depth effect; therefore, no correction factor nor additional computational modeling are necessary. The sample receives its full potential for current density as opposed to a sample that is much thicker than the skin depth. This may explain how static experiments consistently obtain values for electrical resistivity and conductivity that differ by orders of magnitude compared to dynamically determined values of the material.[5,7,42,57,58,68]

II.3. Sample Characteristics and Target Configuration

Weir et al.[56] demonstrated Al_2O_3 to be an excellent insulator to 150 GPa. Thus, two Al_2O_3 (25.4 and 38.2 mm in dia.) were used in each experiment to mechanically constrain and electrically isolate the tin sample. The two Al_2O_3 pieces were Optical Quality HEM Windows (0001) $\pm$ 2° from GT Advanced Technologies (Salem, MA). Electron beam evaporation by Lebow Company (Goleta, CA) was used to deposit 1.6-2.42 μm of Sn on the 38.2 mm Al_2O_3. Tin samples were characterized by a Keyence VK-1000 3D Laser Scanning Confocal Microscope to obtain a sample thickness resolution of 0.5 nm. Information on the conductivity diagnostic can be found in the supplemental materials.[60]

Figure 2(b) provides a schematic of the target assembly. To minimize shunting, shorting, and other potentially adverse effects, no glue was used; the entire sample assembly was mechanically pressed together. A 1 mm thick, 32.83 mm dia. Al 1100 baseplate supported the uncoated side of the 2 mm thick, 38.1 mm dia. Al_2O_3 anvil with the tin deposited film. Thus, the film was on the down range side of the target, in contact with the 25.4 mm dia Al_2O_3 anvil. Cu leads shown in Fig. 2(c) were adhered to the tin sample via silver epoxy (MG Chemicals 8331 Silver Conductive Epoxy Adhesive) to minimize heating the tin sample while maximizing conduction through the junction. Kapton tape and insulating polymers were placed between the Cu leads and the grounded Al target body to isolate the leads. Each lead was soldered to the center conducting wire of a coaxial cable and the cable's shielding was grounded. The coaxial cable was connected to the experimental circuitry. Shorting pins were mechanically pressed downrange of the 25.4 mm dia. Al_2O_3 anvil to provide a trigger to the oscilloscope and a timing fiducial for the experiment for cross-timing analyses. In Table I, the loading parameters, flyer material, and flyer velocity, are provided along with the computationally derived P_{Sn} and T_{Sn} for each of the six experimental results presented herein.

II.4. Computational Modeling

We used computational modeling to predict the shocked P-T-V conditions of the tin sample during the dynamic loading process. A one-dimensional section of Fig. 2(b) was modeled using the ARES hydrocode[69,70] developed at Lawrence Livermore National Laboratory. ARES uses staggered grid hydrodynamics with a second order predictor-corrector time step, and closure is achieved with the Livermore Equation of State (LEOS) library to interpolate tabular EOS data.[71] The model was run with a Lagrangian mesh, which was shown to be first-order accurate in the presence of a shock by testing against the Sod analytical test problem.[70] Local Thermodynamic Equilibrium (LTE) is assumed, while radiative heat transfer is expected to be negligible for temperatures simulated.[72] Thermal conduction is modeled as a diffusion process and the thermal conductivity is taken to be constant over the temperature-density range probed by the experiment.

Equations of state for materials in the one-dimensional model were chosen from the LEOS library. Thermal transport properties for sapphire and tin are not known in the shocked state, thus the thermal conductivity values used in the simulations are set to their ambient values in the CRC handbook.[73] Thermal conduction significantly affects the temperature of the tin sample over the duration of the experiment. Treating the sapphire-tin system as a three layer conduction model with constant thermal diffusivity κ, the conduction time scales as $\tau_d \propto l_{Sn}^2/\kappa_{Sn}$[74] which is comparable to the experimental time scale $\tau_E \propto l_{Al_2O_3}/U_{s,Al_2O_3}$. In future work, improved models estimating the P-T dependence of the thermal conductivity will be used.

II.5. Data Processing

In our experiment, we capture the voltage across the sample, as well as the input current, via the Rogowski coil. To calculate the resistance,[60]

$$R(t) = \frac{V(t)}{I(t)G(I)}. \tag{1}$$

where G(t) is gain, determined by calibrating ambient resistivity and fit to an exponential decay function for its current dependence.[60] To derive electrical resistivity ($\rho(t)$) and conductivity ($\sigma(t)$), we utilize the relationship between the resistance and resistivity which is:

$$R(t) = \rho(t)L_{eff} \tag{2}$$

where L_{eff} is the sample's ambient length, L_0, divided by its cross-sectional area where charge must flow, A_0.

Combining Equations 1 and 2, we obtain

$$\rho(t) = \frac{\eta(t)V(t)}{G(I)L_{eff}I(t)} = \frac{\eta(t)I_0\rho_0V(t)}{V_0I(t)} \tag{3}$$

where $\eta(t)$ is the sample compression under shock conditions. To obtain the electrical conductivity, we invert the electrical resistivity shown in Equation 3,

$$\sigma(t) = \frac{G(I)L_{eff}I(t)}{\eta(t)V(t)} = \frac{V_0I(t)}{\eta(t)I_0\rho_0V(t)}. \tag{4}$$

III. RESULTS AND ANALYSES

Impedance matching and cross-timing were used to find the shock location with respect to the electrical conductivity signal. The signal observed for both $\rho(t)$ and $\sigma(t)$ are corrected for $\eta(t)$, shown in Equations 3 and 4.

Raw ambient and experimental signals for Shot 019 are presented in Fig 3 and 4(b). Projectile impact occurs at $t = 0\ \mu s$, the shock enters the uprange Al_2O_3 at $t = 0.15\ \mu s$, the shock enters the Sn sample at $t = 0.37\ \mu s$, and the experiment ends at $t = 0.6\ \mu s$ due to failure of the target assembly at late times. Signals from -20 to -0.05 μs (before impact) confirm $G(I)$ and L_{eff}.[60]

Figure 4(a) plots the computationally derived P(t) and T(t) for Shot 019. Figure 4(b) shows the voltage output from the Rogowski coil remains nominally constant at 312 ± 0.7 mV, current is 3.12 ± 0.007 A. The voltage signal oscillates from $t = 0.18\ \mu s$ to $t = 0.37\ \mu s$. This is believed to be trapped gasses in the sample target assembly.

For Shot 019, we determined the resistance, resistivity, and conductivity as a function of time, shown in Fig. 5. We focus on a region from 0.415 to 0.595 μs where the sample has reached the steady state after shock at $t = 0.37\ \mu s$, shown by the red markers. The times when the shock wave reaches the different interfaces of the assembly are noted on the plots.

This analysis was repeated for each of the six experiments and results are given in Table I. The electrical resistivity and conductivity calculated for each experiment is shown in Fig. 6(a), (b), (d), and (e). In Fig. 6(a) and (b), resistivity and conductivity were plotted against P while Fig. 6(d) and (e) shows resistivity and conductivity plotted against T. The sample's electrical resistivity and conductivity varies with shock P. There is a trend toward lower resisitivity and higher conductivity values as P increases. But, at 40.8 GPa and 67.2 GPa, there is a discontinuity shown by an increase in resistivity and decrease in conductivity relative to the data points on either side of them. Additionally, though models show T varies with time while samples are at constant P, Fig. 6(d) and (e) shows that the samples maintain a constant resistivity and conductivity.

The discontinuities shown in Fig. 6(a) and (b) provide compelling insight into where solid-to-solid and solid-to-liquid phase boundaries may exist. In the literature, the BCT to BCC phase transition occurs anywhere from 30-45 GPa on the principal Hugoniot.[13,64,75–79] At higher P on the principal Hugoniot, Sn has shown the onset of melting as early as 45 GPa and only fully liquid at P exceeding 70 GPa. Here, we show that there is a decrease in the electrical conductivity at 40.8 GPa and 67.2 GPa, corresponding to the expected BCT to BCC phase and BCC to liquid phase transition boundary, respectively.

Figure 7 shows where all six experiments fall within the tin phase space. Filled circles show the P-T path of the sample during the experiment and are color mapped to the electrical conductivity values at each P-T state. As can be seen, conductivity varies little with T at each P. This diagram includes the melt line from shock melt on release experiments,[77] phase boundaries from shock sound speed experiments,[64,65] and various DAC experimental data.[76,78,79] This visualization demonstrates correlation between the drop in the electrical conductivity and the data point's proximity to a phase boundary.

IV. DISCUSSION

The first observation we make regarding these Sn electrical conductivity experiments is that the electrical conductivity rises as the P-T increase. In contrast, previous experimental results in gas guns and DACs show most metals tend to have a decreasing electrical conductivity with increasing P-T. This could occur for at least two reasons. The first, Sn electrical conductivity has not been explored in these regimes and its response may be different than other metals that have been explored. The second is tied to the skin depth effect for dynamic experiments. As the loading occurs at a higher P state in a gas gun experiment, the effective frequency of the changing resistance is directly related. Thus, as the skin depth decreases with increasing P-T conditions, it would appear to provide a non-corrected resistance that suggests a decreasing electrical conductivity.

A comparison to directly address this trend is the DAC work by Ohta et al.[7] In Ohta's study, they compare their electrical resistivity results to that of Bi et al.[57] which are $\sim$ 4.5x larger than those calculated by Ohta at $\sim$ 212 GPa. In Bi et al. experiments the ambient samples were 0.5 mm thick and compressed to 0.332 mm during the experiment. If we assume Ohta et al.'s results are correct and the reason for the difference with the dynamic data is only the skin depth, we can say that Bi et al.'s effective cross-section is 4.5x smaller. This would yield an effective skin depth of $\sim$ 40 μm and subsequent frequency of $\sim$ 35 kHz in the skin depth calculation.[60] Thus, if the skin depth were properly accounted for in the Bi et al. work, the electrical resistivity would be significantly lower and the electrical conductivity would be significantly higher. This decreasing electrical conductivity obtained dynamically would be substantially influenced by the much smaller effective cross-section that the sample observes due to the skin depth effect not accounted for in previous dynamic studies.

Coupling these electrical conductivity experiments with computational simulations provides valuable insight into the local electronic order of the dynamically compressed Sn. We observe that there are significant discontinuities in the electrical conductivity values when in proximity to a phase boundary. This provides a means to constrain the phase boundary's location, especially important in tin's highly controversial phase diagram. It must first be noted that these data do not fall on the principal Hugoniot of tin. The samples are on the principal Hugoniot for a short time ($< 1\ ns$) since the tin samples are in an Al_2O_3 reservoir and Sn will match $P_{Al_2O_3}$, then thermally equilibriate to the Al_2O_3 T. This provides valu-

able off-Hugoniot data in regions not previously studied to constrain the BCC / BCT and BCC / liquid phase boundaries. The BCC to BCT phase transition occurs in this work between 37 and 45 GPa while the BCC to liquid transformation begins between 45 and 67 GPa.

We explored the T dependence of the electrical conductivity. Figure 6(e) shows a nominally constant electrical conductivity for each of the six experiments when the sample is held at a given P, while T varies during the experiment by up to 1500 K due to thermal equilibriation of the Sn sample with the much colder Al_2O_3 anvils. This suggests that electrical conductivity has no dependence upon temperature, at least in the temperature range probed in this work. This is surprising as the thermal and electrical conductivity pathways are assumed to be the same under these conditions.

Electrical conductivity values from dynamic (gas guns and explosive loading) experiments should be closely analyzed to account for the skin depth effect. Much of the geophysics and astrophysics community has paid close attention to the electrical conductivity of materials at elevated P-T. A current explanation for the magnetic dynamo within Earth is due to the electrical and thermal conductivity of molten Fe. This concept has been much debated as many studies contradict each other regarding the electrical conductivity of Fe. Often in these studies, either electrical conductivity[4,7,24–36] and thermal conductivity[5,32] are solved for and then converted to the other by the Wiedemann-Franz Law. To date, this model is the best approximation that exists using the assumption that thermal and electrical conduction are both disrupted by the coupling of the material's atomic lattice and mobile electrons. Currently, data does not exist at these elevated P-T regimes to test the Wiedemann-Franz Law.

By comparing our electrical conductivity experimental results presented in this work and gas-gun experiments with pyrometry,[41] we are able to directly assess the Wiedemann-Franz Law at $\sim$ 120 GPa. From our electrical conductivity experiments, Sn has an electrical conductivity of 8.51 x 10^4 $[\Omega cm]^{-1}$ and subsequent thermal conductivity from Wiedemann-Franz Law ranging from 0.8 x 10^3 to 1.2 x 10^3 $W[m*K]^{-1}$, shown in Fig. 6(c) and (f). Both plots show a direct relationship between thermal conductivity with the elevated P-T conditions through the inclusion of T in the Wiedemann-Franz law and P's direct relationship with T.

To compare the thermal conductivity values, we modeled the results of FLS1 from Brantley et al.[41] for tin, varying the thermal conductivity values of Sn at elevated P-T to observe the influence on the time dependent T profile. Shown in Fig. 8 are three simulated temperature profiles (dashed lines) that were identical except for their thermal conductivity value, which was varied from the ambient 66 W/mK to 300 W/mK to 1200 W/mK. The computational model employed herein did not fully capture the increased temperature of the gap present in FLS1 that led to the steep rise in the temperature profile for the experimental data. Interestingly, the 1200 W/mK profile happens to show a similar rise in its profile at early times (< 0.02 μs) but failed to capture the proper temperature gradient at later times (> 0.1 μs). The 300 W/mK temperature profile at later times yielded a similar profile to the experimental data but missed the steep rise at early times, as expected since the gap was not included in the simulation. The thermal conductivity of 1200 W/mK, predicted by the Wiedemann-Franz Law yields a temperature significantly larger than what was observed in the FLS1 experiment. Other explanations for the observed descrepancy between model and experiment include incorrect EOS T used in the model, thermal contact resistance, and a probable T-dependence in the thermal conductivity, which was not used in the present models.[80,81] The determination of bulk temperature will show increased uncertainty with increased uncertainties in the thermal conductivity model, including whether it is temperature-dependent; in turn, a lack of knowledge about the true temperature compounds uncertainties in transport. Establishing reliable measurements of the electrical conductivity is a first step. Further discussion into these issues requires further detailed exploration which is beyond the scope of this work but will be addressed in our future publications.

In this work, we showed the importance of considering the skin depth effect in dynamic compaction experiments in metals. We additionally showed that with impedance matched electronics, we were able to obtain excellent signal-to-noise. The results herein show a need to further address the relationship between the thermal and electrical conductivities through high accuracy experiments determining thermal and electrical conductivity independently of each other and developing more advanced models to further understand their relationship to each other. These directed studies would either fully confirm or refute the Wiedemann-Franz Law's applicability and offer alternatives if it is not viable. Work is ongoing by this group to address the relationship of the electrical and thermal conductivities at elevated P-T to allow measurements of bulk T for equation of state determination.

V. ACKNOWLEDGEMENTS

This work was performed under the auspices of the U.S. Department of Energy by Lawrence Livermore National Laboratory under Contract DE-AC52-07NA27344. A special thanks to Elida White, Marylou Manzo, J Castellanos, Dane Ramos, Phil Watts, and Gerard Jacobson aiding in the design and implementation of the experiments. We would like to thank Cory Mclean, Zack Wilkins, Caleb Glickman, and Paul Dealmeida for their help in operating the experiments at the High Energy Application Facility at Lawrence Livermore National Laboratory. We would like to thank Sarah Stewart, Dylan Spaulding, Jill Eymann, and Zach Zentner for their help in operations for the experiments at the UC Davis Shock Lab. We would like to thank Amanda Levasseur for help with figures.

[1] R. Franz and G. Wiedemann, Annalen der Physik **165**, 497 (1853).

[2] N. de Koker, G. Steinle-Neumann, and V. Vlek, Proceedings of the National Academy of Sciences **109**, 4070 (2012).

[3] L. Deng, C. Seagle, Y. Fei, and A. Shahar, Geophysical Research Letters **40**, 33 (2013).

[4] H. Gomi, K. Ohta, K. Hirose, S. Labrosse, R. Caracas, M. J. Verstraete, and J. W. Hernlund, Physics of the Earth and Planetary Interiors **224**, 88 (2013).

[5] Z. Konpkov, R. S. McWilliams, N. Gmez-Prez, and A. F. Goncharov, Nature **534**, 99 (2016).

[6] W. Nellis, Modern Physics Letters B **29**, 1430018 (2015).

[7] K. Ohta, Y. Kuwayama, K. Hirose, K. Shimizu, and Y. Ohishi, Nature **534**, 95 (2016).

[8] R. Scipioni, L. Stixrude, and M. P. Desjarlais, Proceedings of the National Academy of Sciences **114**, 9009 (2017).

[9] M. Pozzo, C. Davies, D. Gubbins, and D. Alfe, Nature **485** (2012).

[10] M. Pozzo, C. Davies, D. Gubbins, and D. Alf, Earth and Planetary Science Letters **393**, 159 (2014).

[11] T. Komabayashi, Journal of Geophysical Research: Solid Earth **119**, 4164 (2014).

[12] J. Xu, P. Zhang, K. Haule, J. Minar, S. Wimmer, H. Ebert, and R. Cohen, Physical review letters **121**, 096601 (2018).

[13] S. Bernard and J. Maillet, Physical Review B **66**, 012103 (2002).

[14] X. Sha and R. Cohen, Journal of Physics: Condensed Matter **23**, 075401 (2011).

[15] F. Stacey and D. Loper, Physics of the Earth and Planetary Interiors **161**, 13 (2007).

[16] F. D. Stacey and O. L. Anderson, Physics of the Earth and Planetary Interiors **124**, 153 (2001).

[17] E. Holmstrm, L. Stixrude, R. Scipioni, and A. Foster, Earth and Planetary Science Letters **490**, 11 (2018).

[18] F. Soubiran and B. Militzer, Nature communications **9**, 3883 (2018).

[19] D. Mukherjee, K. Joshi, and S. C. Gupta, in *Journal of Physics: Conference Series*, Vol. 215 (IOP Publishing) p. 012106.

[20] D. Mukherjee, K. D. Joshi, and S. C. Gupta, AIP Conference Proceedings **1349**, 821 (2011).

[21] I. C. Ezenwa and R. A. Secco, Earth and Planetary Science Letters **474**, 120 (2017).

[22] I. C. Ezenwa and R. A. Secco, Journal of Applied Physics **121**, 225903 (2017).

[23] I. C. Ezenwa and R. A. Secco, High Pressure Research **37**, 319 (2017).

[24] I. C. Ezenwa and T. Yoshino, Review of Scientific Instruments **91**, 023903 (2020).

[25] I. C. Ezenwa and T. Yoshino, Earth and Planetary Science Letters **544**, 116380 (2020).

[26] I. C. Ezenwa and R. A. Secco, Crystals **9**, 359 (2019).

[27] R. E. Silber, R. A. Secco, W. Yong, and J. A. Littleton, Scientific reports **8**, 1 (2018).

[28] R. E. Silber, R. A. Secco, W. Yong, and J. A. Littleton, Journal of Geophysical Research: Solid Earth **124**, 5521 (2019).

[29] R. A. Secco, Physics of the Earth and Planetary Interiors **265**, 23 (2017).

[30] K. M. Bulatov, A. N. Semenov, A. A. Bykov, A. S. Machikhin, K. D. Litasov, P. V. Zinin, and S. V. Rashchenko, High Pressure Research **40**, 315 (2020).

[31] P. Saha, A. Mazumder, and G. D. Mukherjee, Geoscience Frontiers **11**, 1755 (2020).

[32] W.-P. Hsieh, A. F. Goncharov, S. Labrosse, N. Holtgrewe, S. S. Lobanov, I. Chuvashova, F. Deschamps, and J.-F. Lin, Nature communications **11**, 1 (2020).

[33] Y. Zhang, M. Hou, G. Liu, C. Zhang, V. B. Prakapenka, E. Greenberg, Y. Fei, R. Cohen, and J.-F. Lin, Physical review letters **125**, 078501 (2020).

[34] I. C. Ezenwa and T. Yoshino, Icarus **360**, 114367 (2021).

[35] C. T. Seagle, E. Cottrell, Y. Fei, D. R. Hummer, and V. B. Prakapenka, Geophysical Research Letters **40**, 5377 (2013).

[36] W. Yong, R. A. Secco, J. A. Littleton, and R. E. Silber, Geophysical Research Letters **46**, 11065 (2019).

[37] Z. Du, L. Miyagi, G. Amulele, and K. K. Lee, Review of Scientific Instruments **84**, 024502 (2013).

[38] G. Shen, M. L. Rivers, Y. Wang, and S. R. Sutton, Review of Scientific Instruments **72**, 1273 (2001).

[39] S. M. Arveson, B. Kiefer, J. Deng, Z. Liu, and K. K. Lee, Physical Review B **97**, 094103 (2018).

[40] R. A. Fischer, E. Cottrell, E. Hauri, K. K. Lee, and M. Le Voyer, Proceedings of the National Academy of Sciences **117**, 8743 (2020).

[41] D. A. Brantley, R. S. Crum, and M. C. Akin, Journal of Applied Physics **129**, 015903 (2021).

[42] R. Keeler and A. Mitchell, Solid State Communications **7**, 271 (1969).

[43] R. Chau, M. Bastea, A. Mitchell, R. Minich, and W. Nellis, Lawrence Livermore National Laboratory Report (2003).

[44] R. Chau, S. Hamel, and W. J. Nellis, Nature communications **2**, 203 (2011).

[45] R. Chau, A. Mitchell, R. Minich, and W. Nellis, The Journal of Chemical Physics **114**, 1361 (2001).

[46] P. Celliers, G. Collins, D. Hicks, M. Koenig, E. Henry, A. Benuzzi-Mounaix, D. Batani, D. Bradley, L. Da Silva, and R. Wallace, Physics of Plasmas **11**, L41 (2004).

[47] P. Loubeyre, P. Celliers, D. Hicks, E. Henry, A. Dewaele, J. Pasley, J. Eggert, M. Koenig, F. Occelli, and K. Lee, High pressure research **24**, 25 (2004).

[48] A. Mitchell and R. Keeler, Review of Scientific Instruments **39**, 513 (1968).

[49] A. C. Mitchell and W. J. Nellis, The Journal of Chemical Physics **76**, 6273 (1982).

[50] W. Nellis, D. Hamilton, N. Holmes, H. Radousky, F. Ree, A. Mitchell, and M. Nicol, Science **240**, 779 (1988).

[51] W. Nellis, N. Holmes, A. Mitchell, D. Hamilton, and M. Nicol, The Journal of chemical physics **107**, 9096 (1997).

[52] W. Nellis, A. Mitchell, P. McCandless, D. Erskine, and S. Weir, Physical review letters **68**, 2937 (1992).

[53] W. Nellis, S. Weir, and A. Mitchell, Physical Review B **59**, 3434 (1999).

[54] S. Weir, W. Nellis, and A. Mitchell, in *AIP Conference Proceedings*, Vol. 309 (AIP) pp. 881–883.

[55] L. Al'Tshuler, L. Kuleshova, and M. Pavlovskii, Zh. Eksp. Teor. Fiz **39** (1961).

[56] S. Weir, A. Mitchell, and W. Nellis, Journal of applied physics **80**, 1522 (1996).

[57] Y. Bi, H. Tan, and F. Jing, Journal of Physics: Condensed Matter **14**, 10849 (2002).

[58] B. Yan, T. Hua, and J. Fu-Qian, Chinese physics letters **19**, 243 (2002).

[59] J. Wong, R. Linde, and P. De Carli, Nature **219**, 713 (1968).

[60] *See Supplemental Material at [URL will be inserted by publisher] for additional information.*

[61] R. Keeler, in *Physics of High Energy Density*, p. 106.

[62] A. Mandal, B. J. Jensen, M. Hudspeth, S. Root, R. Crum, and M. Akin, Physical Review Materials **4**, 063604 (2020).

[63] C. S. Yoo, N. C. Holmes, M. Ross, D. J. Webb, and C. Pike, Physical Review Letters **70**, 3931 (1993).

[64] J. Hu, X. Zhou, C. Dai, H. Tan, and J. Li, Journal of Applied Physics **104**, 083520 (2008).

[65] P. Song, L.-c. Cai, T.-j. Tao, S. Yuan, H. Chen, J. Huang, X.-w. Zhao, and X.-j. Wang, Journal of Applied Physics **120**, 195101 (2016).

[66] C. Kittel, *Introduction to solid state physics* (1976).

[67] F. Smits, Bell System Technical Journal **37**, 711 (1958).

[68] G. Matassov, *Electrical conductivity of iron–silicon alloys at high pressures and the earth's core*, Report (California Univ., Livermore (USA). Lawrence Livermore Lab., 1977).

[69] R. M. Darlington, T. L. McAbee, and G. Rodrigue, Computer Physics Communications **135**, 58 (2001).

[70] R. N. Rieben, *Prototype Mixed Finite Element Hydrodynamics Capability in ARES*, Report LLNL-TR-405350 (Lawrence Livermore National Lab. (LLNL), Livermore, CA (United States), 2008).

[71] K. Howley, R. Managan, and J. Wasem, Acta Astronautica **103**, 376 (2014).

[72] P. Beck, A. F. Goncharov, J. A. Montoya, V. V. Struzhkin, B. Militzer, R. J. Hemley, and H.-K. Mao, Applied Physics Letters **95**, 096102 (2009).

[73] J. R. Rumble, D. R. Lide, and T. J. Bruno, (2019).

[74] R. Grover and P. A. Urtiew, Journal of Applied Physics **45**, 146 (1974).

[75] R. Briggs, D. Daisenberger, O. Lord, A. Salamat, E. Bailey, M. Walter, and P. McMillan, Physical Review B **95**, 054102 (2017).

[76] S. Weir, M. Lipp, S. Falabella, G. Samudrala, and Y. Vohra, Journal of Applied Physics **111**, 123529 (2012).

[77] C. Mabire and P. L. Hereil, in *AIP Conference Proceedings*, Vol. 505 (AIP) pp. 93–96.

[78] B. Schwager, M. Ross, S. Japel, and R. Boehler, The Journal of chemical physics **133**, 084501 (2010).

[79] B. Kiefer, T. Duffy, T. Uchida, and Y. Wang, APS User Activity Report (2002).

[80] W. Tang, F. Jing, R. Zhang, and J. Hu, Journal of applied physics **80**, 3248 (1996).

[81] T. Hartsfield, B. La Lone, G. Stevens, L. Veeser, and D. Dolan, Journal of Applied Physics **128**, 015903 (2020).

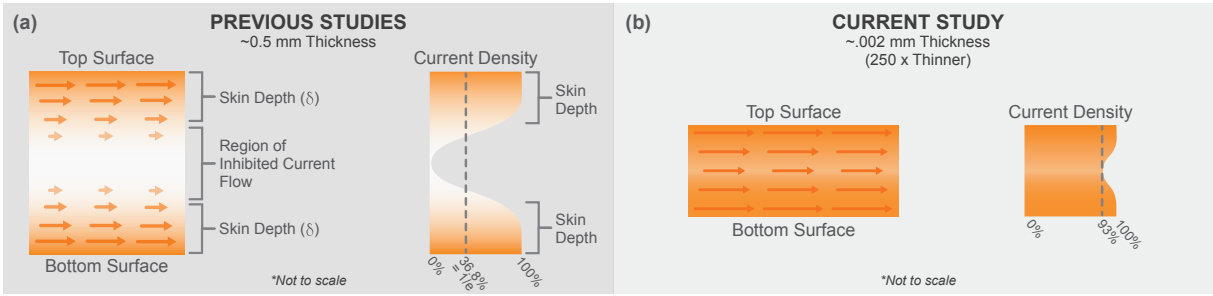

FIG. 1. The skin depth effect shown in (a) a thick sample, larger than the skin depth (δ) and (b) a thin sample with a thickness less than the skin depth (δ). As shown by the color gradient, dark orange demonstrates the full current density while white is a region of no current flow.

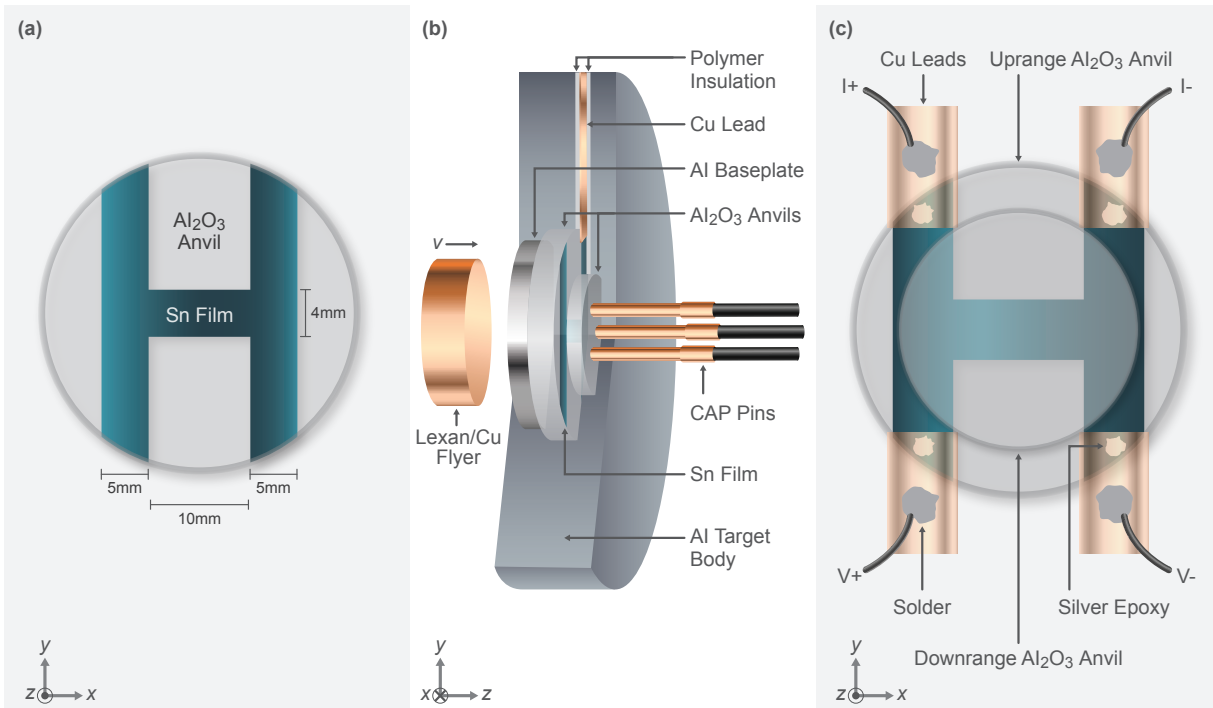

FIG. 2. (a) Schematic of the thin film tin sample coated upon a 38.2mm dia x 2mm thick Al_2O_3 anvil. (b) Schematic of the experimental assembly for the six dynamic experiments. The flyer is launched at the sample from the left and impacts the Al baseplate. (c) Schematic of the target assembly as seen with the projectile coming out of the page. This schematic displays the placement of the Cu leads, silver epoxy, and the downrange Al_2O_3 anvil relative to the coated uprange Al_2O_3.

Experiment Number	Flyer	Velocity $[km/s]$	P $[GPa]$	T $[K]$	h_0 $[\mu m]$	η	L_{eff} $[10^6 \mu m]$	R_0 $[\Omega]$	R $[\Omega]$	ρ $[10^{-7}\Omega * m]$	σ $[10^4[\Omega cm]^{-1}]$
019	Lexan	3.38	24.1	575-480	1.77	0.782	2.02	0.222	0.402	1.56(5)	6.39(21)
018	Lexan	4.62	36.9	1120-600	1.74	0.731	2.25	0.247	0.412	1.35(3)	7.43(19)
4439	Lexan	4.99	40.8	940-745	1.91	0.723	1.80	0.196	0.393	1.57(4)	6.37(18)
4408	Cu	2.32	44.7	1300-800	2.28	0.708	2.08	0.229	0.376	1.21(4)	8.26(25)
4400	Cu	3.21	67.2	2100-1600	2.02	0.655	1.73	0.191	0.388	1.38(4)	7.26(22)
4409	Cu	4.90	117.1	5600-3700	2.28	0.580	1.88	0.207	0.407	1.17(4)	8.51(26)

TABLE I. The experimental and simulation values for the six experiments. The pressure (P), temperature (T), and compaction (η) are determined via impedance matching and 1-D computational models. The temperature range shown here is from the beginning of data collection to the end for the given experiment. The gain (G) and effective length (L_{eff}) are determined from the experimental ambient state. The h_0 and R_0 are measured for the sample prior to the experiment. The experimental resistance (R), electrical resistivity (ρ), and electrical conductivity (σ) are determined from the experiment.

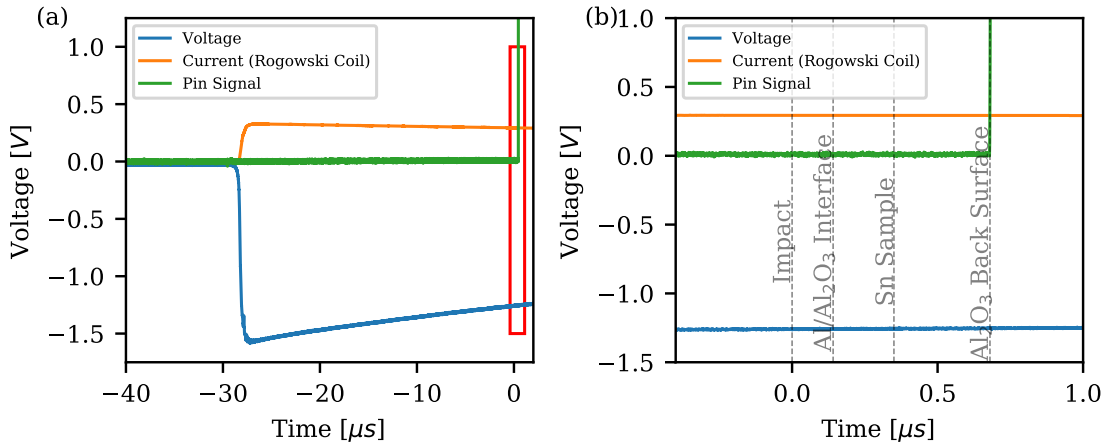

FIG. 3. Voltage, current (Rogowski coil), and shorting pin signals for an ambient sample dry run. (a) Shows the signals from when the circuit triggers until the experiment takes place. The red box in (a) is enlarged in (b) to show the ambient signals during the duration of the shock loading experiment. The vertical gray lines are presented to show the experimental timings of shock wave's location within the experimental assembly for experiment 019. As the shock wave reaches the back surface of the downrange Al_2O_3 anvil, the cap pins that are in contact with the back surface are triggered. As shown in (b), the current from the Rogowski coil and subsequent sensing voltage remains effectively constant on this timescale.

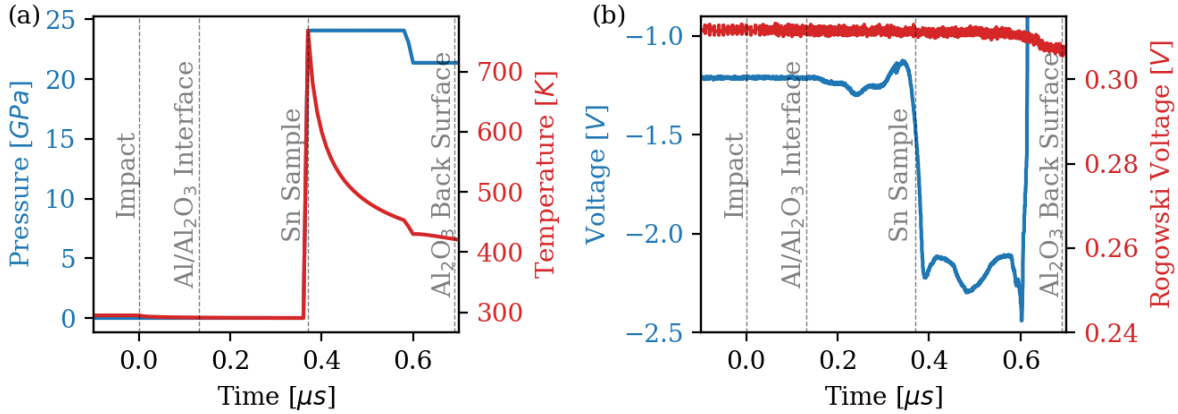

FIG. 4. (a) The computationally derived pressure and temperature profiles within the tin sample for Shot 019. (b) Raw experimental voltage from the differential amplifier and the Rogowski coil voltage, both from Shot 019. The computationally expected times for the shock transit location are labelled in both (a) and (b).

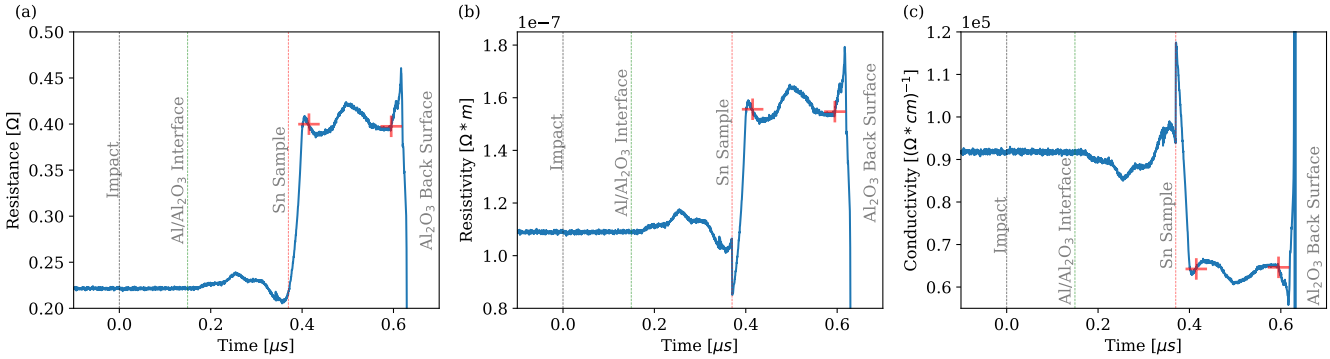

FIG. 5. (a) Corrected resistance vs. time from shot 019. (b) Corrected electrical resistivity vs. time from shot 019. (c) Corrected electrical conductivity vs. time shot 019. The red markers are the regions where the dynamically loaded experimental data was analyzed.

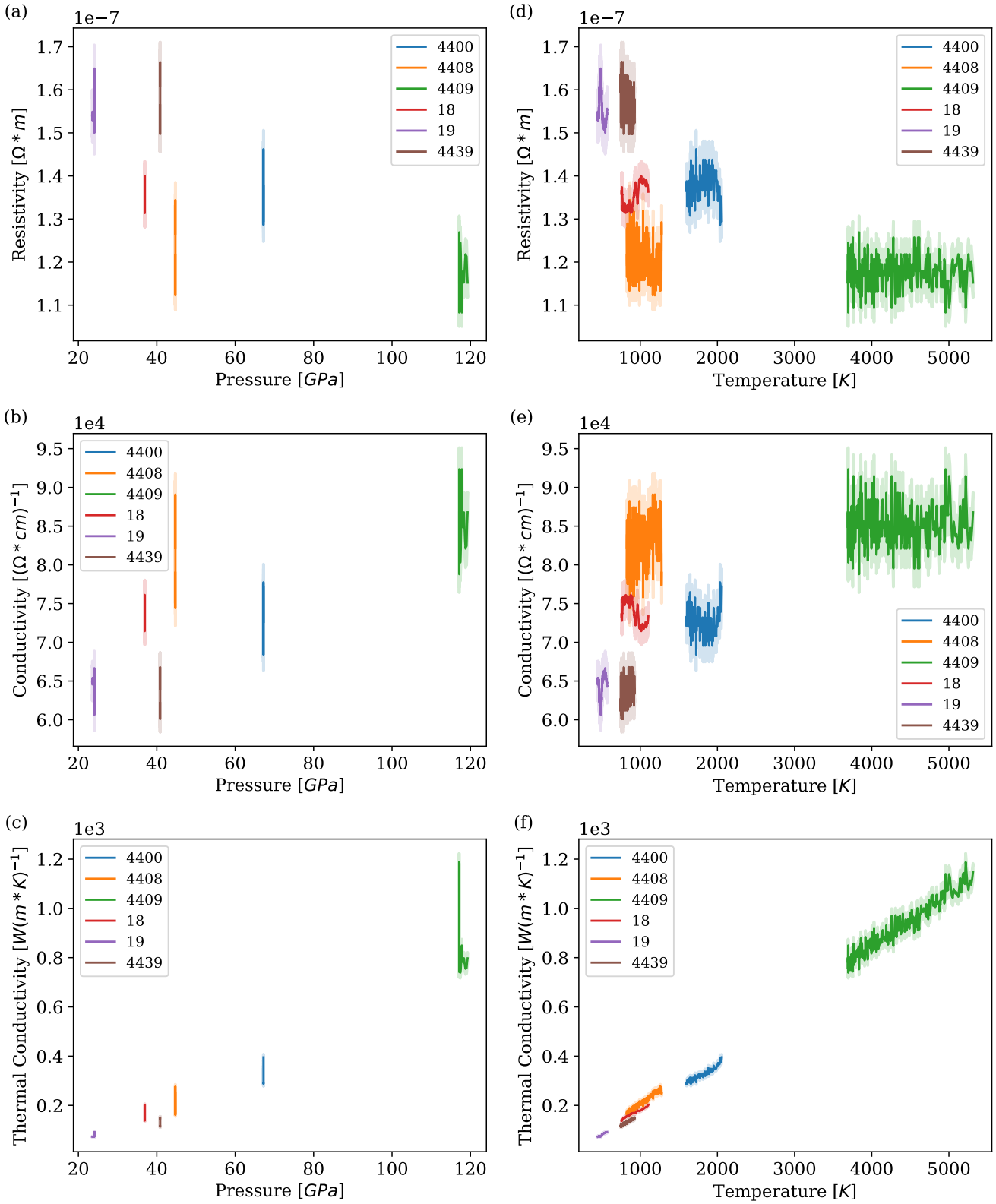

FIG. 6. (a,d) The electrical resistivity, (b,e) electrical conductivity, and (c,f) thermal conductivity vs. pressure and temperature, respectively. The thermal conductivity is calculated from the Wiedemann-Franz Law and the computationally derived temperature using LEOS . Error bounds are shown with transparent region accompanying each data set.

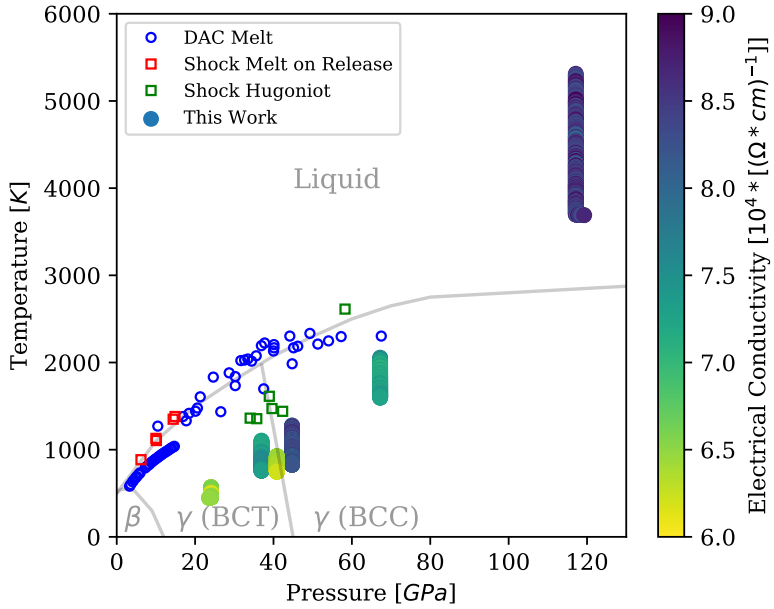

FIG. 7. The computationally derived pressure and temperature conditions of the sample at equilibrium for each experiment in this study overlayed upon the Sn phase diagram (gray lines). Beside each experimental point from this study is its electrical conductivity value as derived in the experiments herein. Additional data points of the melt line from shock melt on release experiments,[77] phase boundaries from shock sound speed experiments,[64,65] and various DAC experiments.[76,78,79]

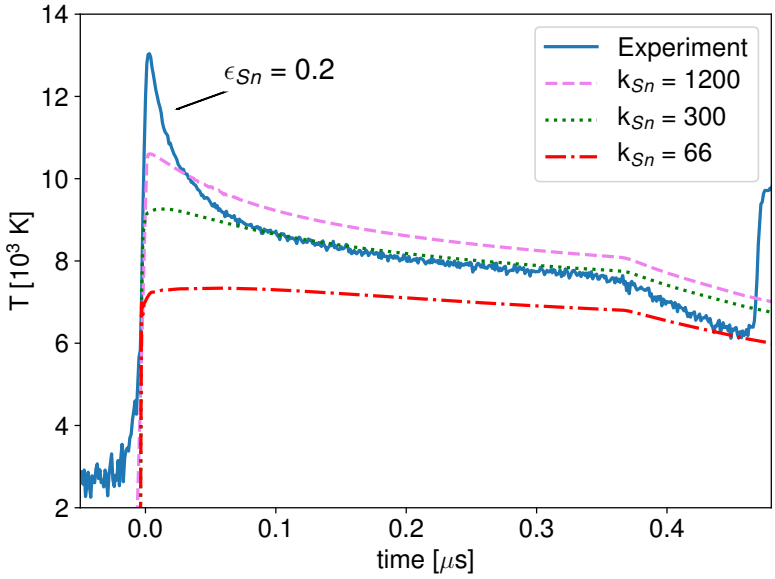

FIG. 8. Data from the Brantley et al.[41] where Sn was shocked to $\sim 120\ GPa$. This experiment was modeled with three different thermal conductivity values, 66 W/mK, 300 W/mK, and the Wiedemann-Franz Law derived 1200 W/mK from this study.